AE3212-II Structural Technical Report

Group A01

Wieger Vellema	4443438
Maartje Duzijn	4486285
Michael Westheim	4355636
Robert Kooij	4444531
Sieglinde Goossenaerts	4291093
Alberto Bonifazi	4431057

March 2, 2018

Faculty of Aerospace Engineering

TU Delft Delft University of Technology

Challenge the future

Contents

Contents ii

1 Introduction 1

2 Problem Analysis 2
- 2.1 Description of the Aileron . . . 2
- 2.2 Critical Load Scenario . . . 3
- 2.3 Input & Output Variables . . . 5

3 Assumptions 6

4 Theoretical Background 8
- 4.1 Reaction Forces and Moments . . . 8

5 Analytical Model 10
- 5.1 Area Characteristics . . . 10
  - 5.1.1 Centroid . . . 10
  - 5.1.2 Moments of Inertia . . . 10
  - 5.1.3 Shear Center . . . 11
- 5.2 Forces and Moments . . . 11
- 5.3 Shear Flow and Torsion . . . 12
  - 5.3.1 Shear Flow . . . 12
  - 5.3.2 Torsion . . . 12

6 Numerical Model 13
- 6.1 Area Characteristics . . . 13
  - 6.1.1 Boom Areas . . . 13
  - 6.1.2 Centroid . . . 13
  - 6.1.3 Moments of Inertia . . . 14
- 6.2 Forces in Y-Direction . . . 14
- 6.3 Internal Forces . . . 15
- 6.4 Shear and Torsion . . . 16
  - 6.4.1 Shear Flows . . . 16
  - 6.4.2 Torsion . . . 17

7 Verification 18
- 7.1 Code Verification . . . 18
- 7.2 Unit Tests . . . 19
- 7.3 System Test . . . 24

8 Validation 25
- 8.1 Experimental Data . . . 25
- 8.2 Validation Test . . . 25
- 8.3 Accuracy of Results . . . 25
- 8.4 Evaluation . . . 27

9 Conclusion 28

10 Group Organisation 29

11 Appendix A: Code **31**

Nomenclature

$\bar{x}$	x-coordinate of the centroid	m
$\bar{y}$	y-coordinate of the centroid	m
$\bar{z}$	z-coordinate of the centroid	m
θ	Angle of deflection of the aileron	deg
$\tilde{x_i}$	x-coordinate of the center of the area of part i	m
$\tilde{y_i}$	y-coordinate of the center of the area of part i	m
$\tilde{z_i}$	z-coordinate of the center of the area of part i	m
t_{sk}	Skin thickness of the aileron	mm
x_1	x-location of hinge 1	m
x_2	x-location of hinge 2	m
x_3	x-location of hinge 3	m
x_a	Distance between actuator 1 and 2	m
σ_r	Normal stress in boom r	N/m^2
$\sum F_x$	The sum of the forces in x-direction	kN
$\sum F_y$	The sum of the forces in y-direction	kN
$\sum F_z$	The sum of the forces in z-direction	kN
$\sum M_x$	The sum of the moments in x-direction	$kN \cdot m$
$\sum M_y$	The sum of the moments in y-direction	$kN \cdot m$
$\sum M_z$	The sum of the moments in z-direction	$kN \cdot m$
A	Constant of integration	-
A_i	Contributing area of part i	m^2
B	Constant of integration	-
B_r	Boom area of boom r	m^2
C	Constant of integration	-
C_1	Constant in integration	-
C_2	Constant in integration	-
C_3	Constant in integration	-
C_a	Chord length of the aileron	m

D	Constant of integration	-
d_1	Vertical displacement at hinge 1	m
d_3	Vertical displacement at hinge 3	m
d_3^z	Displacement at hinge 3 in z-direction	m
E	Young's modulus	GPa
F_I^z	Resultant force applied by actuator 1	kN
G	Shear modulus	Pa
h	Aileron height	m
I_{yy}	Moment of inertia around the y-axis	m^4
I_{yz}	Product moment of inertia around the y and z-axis	m^4
I_{zz}	Moment of inertia around the z-axis	m^4
l_a	Length of the aileron	m
M	Moment [kNm]	
P	Load in actuator 2	kN
q	Net aerodynamic load	kN/m^2
q_s	Shear flow	n/m
R_1^x	Reaction force in hinge 1 in x-direction	kN
R_1^y	Reaction force in hinge 1 in y-direction	kN
R_1^z	Reaction force in hinge 1 in z-direction	kN
R_2^x	Reaction force in hinge 2 in x-direction	kN
R_2^y	Reaction force in hinge 2 in y-direction	kN
R_2^z	Reaction force in hinge 2 in z-direction	kN
R_3^x	Reaction force in hinge 3 in x-direction	kN
R_3^y	Reaction force in hinge 3 in y-direction	kN
S_y	Distance to the y-location of the shear center	m
S_z	Distance to the z-location of the shear center	m

1 Introduction

The main challenge in the field of flight dynamics is the goal to design an aircraft which is both agile, or eager to realize an altitude change in a specific amount of time, and stable as well. In order to achieve these objectives, an aircraft in general is equipped with different control surfaces. A specific type of control surface is the aileron, which enables the pilot to control the aircraft along its longitudinal axis. A wing often has two ailerons, which are located close to the tips of the wing. The rolling movement is achieved by a concurrent motion: while one goes up decreasing lift, the other goes down increasing it. A correct operation of this surface is critical. In fact, a flaw in this structure is a risk for flight safety.

In order to ensure a correct operation of the aileron, a stress analysis has to be performed for different critical loading scenarios. This project analyzes such a situation for a Boeing 737. In particular, a detailed analysis is performed on the case in which the wing is subject to the maximum aerodynamic load, one of the two actuators of the aileron is jammed, and the aileron is at maximum upward deflection. In this case, the aileron is loaded in torsion, bending and shear.

This report presents the numerical structural analysis tool that will be used to perform the analysis. The tool is able to compute the maximum deflection of the leading edge and the trailing edge of the aileron. In addition, the maximum shear stress and normal stress at critical locations is an output. First, an analysis of the problem can be found under chapter 2. The assumptions made concerning the analysis are listed in chapter 3. Under chapter 5, an analytical model is presented to verify the results of the numerical tool, which in its turn can be found under chapter 6. Finally, a verification and validation method of the numerical model is proposed in chapter 7 and chapter 8 respectively.

2 | Problem Analysis

The problem can be synthetically summarized as follow: "Compute the maximum deflection of the leading edge and trailing edge of the aileron, and the maximum shear flow in the ribs" (van der Wal and Campen, 2018). In order to solve this problem, a correct analysis of the load scenario is crucial. In this chapter, the structure of the aileron is presented, an analysis of the different forces acting on the aileron is performed using a free body diagram, and the input and output variables are discussed.

2.1 Description of the Aileron

The aileron is from a Boeing 737 and it is made of aluminum 2024-T3. It has a semicircular leading edge, a spar and a triangular trailing edge. It has 15 stiffeners uniformly distributed along the skin of the aileron and they run over his full length. The aileron is symmetric with respect to the z-axis. The cross-section of the aileron is shown in Figure 2.1 (van der Wal and Campen, 2018).

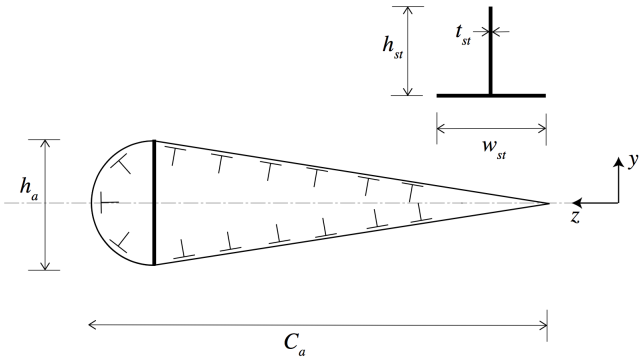

Figure 2.1: Cross-section of aileron and stiffener geometry, (van der Wal and Campen, 2018).

Furthermore, the aileron is hinged at three points, numbered 1 to 3. It has two actuators, named I and II, and four ribs, A, B, C and D. The two actuators are at the same x-distance from hinge 2. The XZ-plane is shown in Figure 2.2 (van der Wal and Campen, 2018).

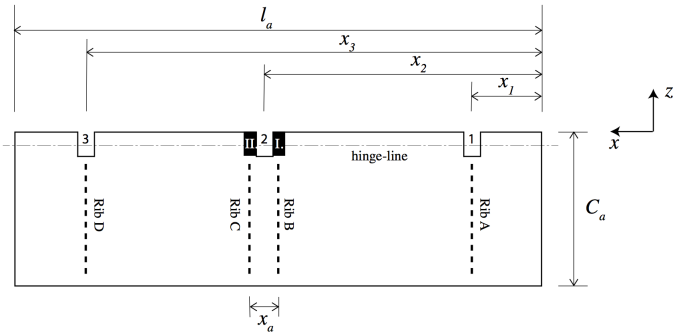

Figure 2.2: XZ-plane of aileron, (van der Wal and Campen, 2018).

2.2 Critical Load Scenario

The critical load scenario analyzes the wing subjected to the maximum aerodynamic load and the aileron at maximum upward deflection with one of the two actuators jammed. In this case, the aileron is loaded in torsion, bending and shear. More specifically the aileron is hinged at 3 points, and an overview of the load case is as follows (van der Wal and Campen, 2018):

- Hinge 1 is fixed in x- and z-direction, and displaced in y-direction by a predefined amount. The force in y-direction is caused by the bending of the wing.
- Hinge 2 is fixed in x-, y- and z-direction.
- Hinge 3 is fixed in x- direction and displaced in y-direction by a predefined amount. The force in y-direction is caused by the bending of the wing.
- Actuator I is kept fixed in z direction.
- Discrete load P acts in negative z-direction at actuator II.
- Distributed load q applied at a quarter of its chord. The load is due to aerodynamic forces on the aileron, it points in negative y-direction and it remains constant irrespective of aileron deformation.

The free-body diagrams for this scenario are displayed in Figure 2.3, Figure 2.4 and Figure 2.5. In Figure 2.3, 1, 2 and 3 refers to the position of the different hinges, precisely displayed in Figure 2.2. I and II are the points of application of the actuators, they are aligned with rib B and rib C respectively, for a more precise representation: Figure 2.4. The forces are indicated in red, where R refers to a reaction force. Although hinge 1 and 3 are not restricted in y-direction, there is a reaction force in y-direction at both hinges which corresponds with the force that causes the initial vertical displacement. The actual displacements are shown in Figure 2.5.

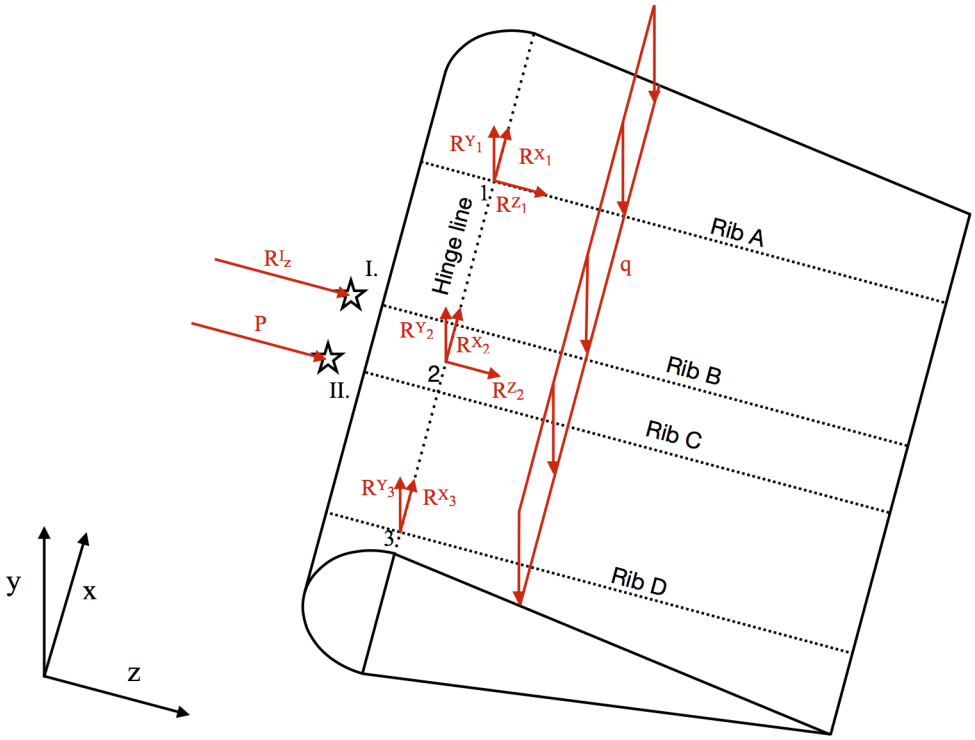

Figure 2.3: Free body diagram for the described loading scenario.

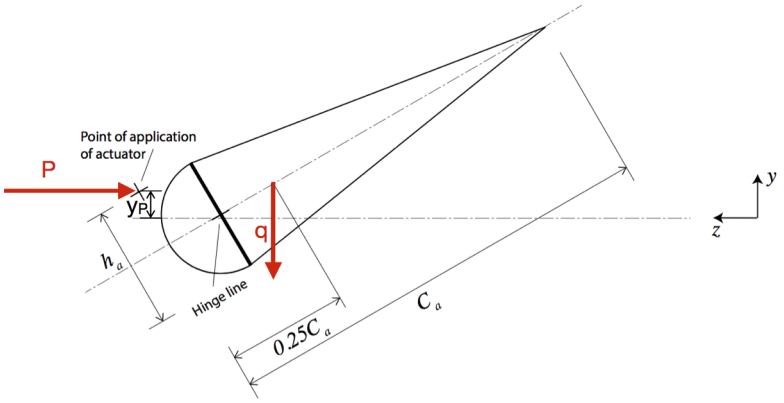

Figure 2.4: Point of application of actuator with deflected aileron.

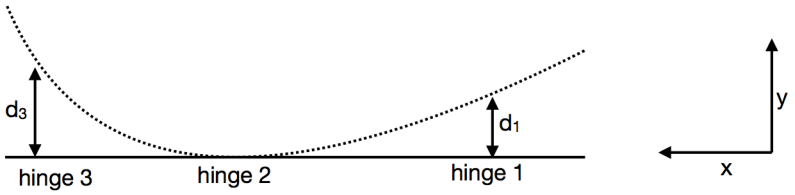

Figure 2.5: Deformed aileron, showing displacement of hinges.

2.3 Input & Output Variables

The input variables are used for both models, the analytical and the numerical. The input variables are geometrical properties of the aileron, the forces acting on it and the material properties (van der Wal and Campen, 2018). Ultimately, the model will provide for the maximum deflection of the leading edge and trailing edge of the aileron, the maximum shear stress and normal stress, and the critical locations of the structure.

The output variables are shown in Table 2.1. Ultimately, the model provides the maximum deflection of the leading edge and trailing edge of the aileron and the maximum shear flow in the ribs.

Output variables aileron Boeing 737		
Property	**Symbol**	**Unit**
Displacement force at hinge 1	D1y	kN
Reaction force Z at hinge 1	R1z	kN
Reaction force X at hinge 1	R1x	kN
Reaction force Y at hinge 2	R2y	kN
Reaction force Z at hinge 2	R2z	kN
Reaction force X at hinge 2	R2x	kN
Displacement force at hinge 3	D3y	kN
Reaction force X at hinge 3	R3x	kN
Reaction force at actuator I.	Rz	kN
Stress distribution due to normal forces	σ	Pa
Stress distribution due to bending moment	σ	Pa
Moment of inertia around z-axis	I_{zz}	m^4
Moment of inertia around y-axis	I_{yy}	m^4
Shear flow distribution due to shear forces	q	kN/m
Shear flow distribution due to torsion	q	kN/m
Torque	T	kNm
Maximum shear flow in ribs	q	kN/m
Maximum deflection leading edge aileron	$d_{leading}$	deg
Maximum deflection trailing edge aileron	$d_{trailing}$	deg

Table 2.1: Output variables used for the analysis.

3 | Assumptions

In this chapter a list of assumptions is given which are used regarding the analytical and numerical model of the aileron. In addition, the influence every assumption has on the end result is stated as well.

1. Concerning the material and geometry of the aileron, the following general assumptions can be made. Assumption 1c to 1e are based on the instruction manual of the course AE3212-II (van der Wal and Campen, 2018).

   (a) The aileron is assumed to be made of perfectly isentropic material: no anomalies present at the skin or any other imperfect mass distributions. The values given are constant throughout the aileron. The effect on our model means imperfections are not accounted for. However, the presence of imperfections is expected to make the material properties marginally worse than assumed.

   (b) The material will only deform elastically. This means the material will behave linear with its E-modulus, and after loading the aileron will return to its original shape. It is unlikely that this would have much effect on the model since we consider high quality materials that have been extensively tested before.

   (c) The aileron is considered to be a beam. Therefore, in the analytical model, the formulas for deflections due to the bending of an asymmetrically loaded beam as given by Megson (2013) are assumed to be valid.This may introduce some local effects but as it is widely used in engineering, the effects will be sufficiently small.

   (d) Under the critical load case described, the cross-section of the aileron is assumed to be constant throughout its length, and the x-z plane can be considered a symmetry plane of the aileron for any chunk dx considered sufficiently small. For this reason, the bending, torsion and shear loads can be assumed independent of each other and super-position can be used. This also means the angle of twist is constant for an entire multi-cell. As a result, there is not accounted for a change in moments of inertia, but these effects will be small.

   (e) The stiffeners are uniformly distributed along the circumference of the aileron and run over the full length of the aileron. The attachments of the stiffeners to the skin of the aileron are not of any influence on the given load case. No structural degradation due to riveting is assumed. The effect of this assumption might be considerable.

   (f) The cut-outs due to the hinges in the skin panels of the aileron (when looking from the x-z plane) are neglected. This is a valid assumption since the cut-outs will be filled with material from the actuator.

   (g) The aileron is assumed to be a thin-walled structure, since the dimensions of the skin are typically 100 times smaller than the other dimensions (Hibbeler, 2014).

2. The aileron is hinged at three points with two actuators attached in the middle (van der Wal and Campen, 2018). Concerning the hinge points and the actuators, the following assumptions are made:

   (a) The hinges are assumed to only restrict translations, but allow rotations in all directions for small angles. As a result, a hinge point cannot create a moment onto the aileron. Therefore, in the bending analysis, the aileron can be cut at hinge 2 and clamped at

that location. The reaction moment at the clamp will equal the internal moment at that location (van der Wal and Campen, 2018).

(b) The reaction loads at the hinges and actuators can be modelled as point loads (van der Wal and Campen, 2018). This may result in slightly higher stresses in the structure.

(c) The aileron is subject to a bending displacement, since the wing is under limit load. This displacement causes an initial vertical displacement at hinge points 1 and 3. The middle hinge point, hinge 2, is kept fixed (van der Wal and Campen, 2018). It is assumed that the displacement caused by any bending, shear or torque can be superimposed on this initial vertical displacement. In addition, the vertical y displacement is assumed not to have influence on the geometry in the x-z plane. Superposition does not account for the interaction between the forces so these effects might be of influence.

(d) It is assumed that the torque created by the actuators does not have any influence on the bending of the aileron in the x-z plane. However, in reality, the reaction forces due to bending might differ from the analytical model.

3. When modelling the model numerically, idealization of the structure is assumed. This means that the stringers, spars and ribs are replaced by concentration of areas, also known as booms (Megson, 2013). This implies the following:

   (a) The skin is only effective in resisting shear stress, while the booms take up all the direct stresses. This will result in an underestimation of the bending stiffness.

   (b) The boom area corresponds with the capacity of the stringers, spars and ribs to take up any direct stresses. Due to the lower bending stiffness, the maximum normal stress will be overestimated.

   (c) The ratios between the direct stress distribution when calculating the boom areas, is assumed to be 1 for an axial load and -1 for a pure bending moment (Megson, 2013). Furthermore, it is assumed that the ratios of the direct stress distribution can be determined by using the distance from the centroid, since the normal stress is assumed to be linear. This does not take variations of normal stresses within the boom into account.

   (d) The ribs are assumed to only introduce extra area into the booms. The booms idealization still holds. This is a significant assumption and will introduce some local discrepancies.

   (e) In order to calculate the location of the centroid, only the boom areas are used to find the coordinates. The centroid is therefore in a slightly different position.

   (f) The idealized moments of inertia are calculated by considering a Steiner term only. This means they are underestimated, as is the bending stiffness.

   Idealizing the aileron will have effect on the maximum shear stress and maximum deflection of the leading and trailing edge. The idealization will lead to a constant shear flow over the skin and the ribs, which results in an underestimation of the maximum shear flow.
   Concerning the bending stiffness, this will be underestimated due to the fact that the contribution of the skin is neglected. As a result of the underestimated bending stiffness, the maximum normal stress will be overestimated. The idealization of this structure is valid, since shear is typically less critical than normal stress in a thin-walled structure (Megson, 2013).

4. Concerning the loading case and failures that may occur during loading, another few assumptions are made:

   (a) It is assumed that premature failure of (sub) parts of the aileron will not occur during the test. In addition, phenomena such as fatigue, crack growth, buckling and crippling are not accounted for. If this does occur during the test, it means the aileron overall is poorly designed and overestimated in general. These effects should be determined in subsequent tests.

4 | Theoretical Background

This chapter offers the theoretical background common to the two models.

4.1 Reaction Forces and Moments

The next step in resolving for the mechanical response of the structure is to find the reaction forces and moments. In order to find the sum of forces and moments in x, y and z direction, the FBD-diagram of the system is used (Figure 2.3 as stated in section 2.2). Since the aileron is not moving, static equilibrium is assumed. As a consequence, the sum of forces and moments have to equal zero. Both the sum of forces and sum of moments are presented by Equation 4.1 and Equation 4.2. Note: the sum of moments is taken around hinge 2 for all directions.

$$\begin{aligned} \sum F_x &= R_1^x + R_2^x + R_3^x = 0 \\ \sum F_y &= R_1^y + R_2^y + R_3^y - q \cdot l_a = 0 \\ \sum F_z &= R_1^z + R_2^z + P + F_I^z = 0 \end{aligned} \tag{4.1}$$

$$\begin{aligned} \sum M_x &= \frac{Ph_a}{2}(cos\theta - sin\theta) + \frac{F_I^z h_a}{2}(cos\theta - sin\theta) + R_1^z d_1 + \\ &\quad ql_a\left(0.25C_a - \frac{h_a}{2}\right)cos\theta - R_3^y \cdot d_3^z = 0 \\ \sum M_y &= -R_1^z(x_2 - x_1) + (P - F_I^z)\frac{x_a}{2} + R_3^x \cdot d_3^z = 0 \\ \sum M_z &= -R_1^x d_1 - R_3^x d_3 + q\left(\frac{l_a^2}{2} - x_2 l_a\right) + R_1^y(x_2 - x_1) - R_3^y(x_3 - x_2) = 0 \end{aligned} \tag{4.2}$$

4.1.0.1 Rotating the Moment of Inertia

Before continuing with the computation of the reaction forces, it has to be mentioned first that the aileron is now at an angle θ. As a consequence, the moment of inertia as computed in section 5.1 has to be rotated as well. This is done by the relation as stated in Equation 4.3 (Kwon, 1998).

$$\begin{aligned} I_{rotated} &= R^T \cdot I_{tensor} \cdot R \\ R &= \begin{bmatrix} \cos\theta & \sin\theta \\ -\sin\theta) & \cos\theta \end{bmatrix}, I_{tensor} = \begin{bmatrix} I_{yy} & 0 \\ 0 & I_{zz} \end{bmatrix} \\ I_{rotated} &= \begin{bmatrix} I_{yy} & I_{yz} \\ I_{zy} & I_{zz} \end{bmatrix} \end{aligned} \tag{4.3}$$

In the reaction and internal force calculations, the rotated moments of inertia are used.

4.1.0.2 Forces in X-Direction

From the FBD-diagram as shown in Figure 2.3 (chapter 2), it can be seen that at all three hinges, there will be a reaction force in the x-direction due to the bending of the aileron. However, since there

is no external force in x-direction, it is assumed that the reaction forces in x-direction are negligible small in comparison to the other reaction forces. This assumption can be considered valid, since the length l_a of the aileron does not change significantly when loading the system. The length $x_2 - x_1$ and $x_3 - x_2$ change -0.62% and -0.89% respectively (Figure 4.1). Therefore, the forces in x-direction can safely be assumed to be negligible small. As a consequence, the reaction forces in x-direction will be neglected in further calculations.

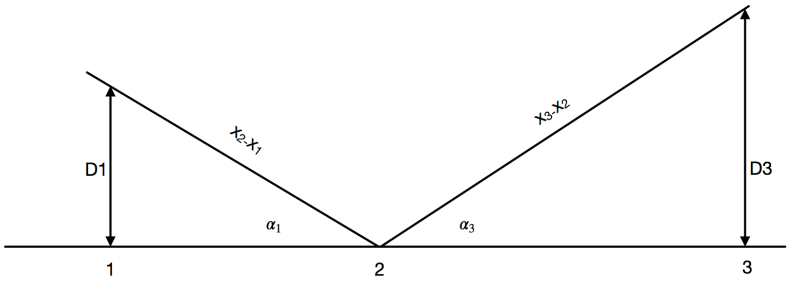

Figure 4.1: Geometry of the deflection of the wing.

4.1.0.3 Forces in Z-Direction

In Equation 4.1 and Equation 4.2, the sum of the forces and the sum of the moments in all directions are given. Looking at the these equations, it can be concluded that the sum of forces in z-direction and the sum of moments in x- and y-direction solely depend on the forces in z-direction. Combining this with the fact that the the system only has three unknown in z-direction, R_1^z, R_2^z and F_I^z, the system is statically determinant for the forces in z-direction.To solve for the forces in the z-direction, the sum of forces in z-direction and the sum of moments around the y- and x-axis are combined. This results in the linear system described in Equation 4.4, where $\boldsymbol{w}$ is the vector with the unknowns R_1^z, R_2^z and F_I^z.

$$
\begin{aligned}
&A\boldsymbol{w} = \boldsymbol{k} \\
&A = \begin{bmatrix} 1 & 1 & 1 \\ (x_2 - x_1) & 0 & \frac{x_a}{2} \\ d_1 & 0 & \frac{h_a}{2}(cos\theta - sin\theta) \end{bmatrix}, \quad \boldsymbol{w} = \begin{bmatrix} R_1^z \\ R_2^z \\ F_I^z \end{bmatrix} \\
&\boldsymbol{k} = \begin{bmatrix} -P \\ \frac{x_a \cdot P}{2} \\ \frac{P \cdot h_a}{2}(sin\theta - cos\theta) + q \cdot l_a(\frac{h_a}{2} - \frac{1}{4}C_a)cos(\theta) \end{bmatrix}
\end{aligned} \tag{4.4}
$$

Solving the system as described in Equation 4.4 will result in the values for R_1^z, R_2^z and F_I^z. In the next section, these forces are assumed to be known from now on, in order to find the remaining (unknown) reaction forces (the forces in y-direction).

5 | Analytical Model

In this chapter, an overview is given of the analytical method which is used to describe the mechanical response of the structure in a mathematically closed form. This method is eventually used to verify the outcome of different parts of the numerical model, as given in chapter 6. For this reason, this chapter is divided in several (sub)sections which may be used separately to check the outcome of the numerical model. The problem analysis is entirely like the one given in the simulation plan.

5.1 Area Characteristics

In order to check the influence of the assumptions used for the numerical model concerning the area characteristics, the area characteristics of the structure are calculated analytically as well. For the analytical model, the centroid and moments of inertia are calculated as is taught in courses like Mechanics of Materials (Hibbeler, 2014).

In this section, the area characteristics of the aileron are calculated as if the aileron is not rotated yet. Eventually, in section 4.1, an explanation will be provided on how the area characteristics are computed for the rotated aileron.Concerning the area characteristics, especially assumption 1a (isentropic material), 1d (constant cross-section) and 1g (thin-walled structure), which can be found under chapter 3.

5.1.1 Centroid

In the analytical model, the location of the centroid depends on all the different parts of the structure, including for example the contribution of the skin and the stringers. As in Mechanics of Materials, Equation 5.1 is used (Hibbeler, 2014).

$$\bar{y} = \frac{\Sigma A_i \tilde{y_i}}{\Sigma A_i} \qquad\qquad \bar{z} = \frac{\Sigma A_i \tilde{z_i}}{\Sigma A_i} \tag{5.1}$$

This formula is used straightforwardly when calculating the contribution of the skin, spar and stiffeners to the location of the centroid. However, for the semicircular leading edge, the z-location is determined using Equation 5.2 (Hibbeler, 2014). Due to symmetry, the y-location of the centroid is not of interest.

$$\bar{z}_{semicircularLE} = \frac{2r}{\pi} \tag{5.2}$$

5.1.2 Moments of Inertia

The skin, stringers and ribs all contribute to the moment of inertia in both mass and Steiner terms. Because the cross-section z-y is considered thin-walled, only the lowest order of the t terms are taken into account (chapter 3, item 1g). To find the moments of inertia, Equation 5.3 is used in the z-y plane.

$$I_{zz} = \int_A y^2 \, dz \, dy \tag{5.3}$$

From Equation 5.3, the moment of inertia can be derived for a thin plate at an angle. Except for the semicircular leading edge, all the different parts of the cross-section in the z-y plane can be considered as thin plates at an angle (skin plate, the stiffener components and the spar). In order to calculate the moment of inertia of an inclined skin section at an angle β, length a and thickness t, Equation 5.4 is used (Megson, 2013). For each skin section, the Steiner term needs to be added as well.

$$I_{zz} = \frac{a^3 t sin^2\beta}{12} \qquad I_{yy} = \frac{a^3 t cos^2\beta}{12} \qquad I_{zy} = \frac{a^3 t sin\beta cos\beta}{12} \tag{5.4}$$

For the semicircular section, Equation 5.5 can be used to find the moment of inertia of the cross-section (Megson, 2013). This formula holds for a thin-walled structure.

$$I_{zz} = \int_0^{\pi r} ty^2\, ds = \int_0^{\pi} t\,(r\cos\theta)^2\, r\, d\theta = \frac{\pi r^3 t}{2} = I_{yy} \tag{5.5}$$

For the moment of inertia around the y-axis of the semicircular leading edge, the moment of inertia is taken about the center of the circle. When computing the total moment of inertia, it needs to be taken into account that a Steiner-term is added for the semi circle from the middle point of the structure to the location of the centroid of the total structure. Since there is an axis of symmetry in the structure, the moment of inertia of the semicircular leading edge around the z-y axis equals zero.

5.1.3 Shear Center

To determine the shear center location, the centroid and moments of inertia are used as determined in subsection 5.1.1 and subsection 5.1.2. Because the cross-section is symmetric in the z-y plane (item 1d in chapter 3), I_{zy} equals zero. Therefore, the shear center will be located on the z axis. To find ζ_0, the location of the shear center on the z-axis, the virtual forces S_y and $S_z = 0$ are applied as in Equation 5.6. Two cuts are made in the structure and the cells are evaluated as if they are open. In this way it is possible to find the base shear flow q_b for both cells. In the skin where the cut is made, q_b is zero.

$$q_s = -\left(\frac{S_z I_{zz} - S_y I_{yz}}{I_{zz} I_{yy} - I_{yz}^2}\right) \int_0^s tz\, ds - \left(\frac{S_y I_{yy} - S_z I_{yz}}{I_{zz} I_{yy} - I_{yz}^2}\right) \int_0^s ty\, ds + q_b \tag{5.6}$$

Subsequently, $q_{s,0}$ is determined for both cells using Equation 5.7.

$$q_{s,0} = \frac{\oint \frac{q_b}{Gt}\, ds}{\oint \frac{1}{Gt}\, ds} \tag{5.7}$$

The found values for $q_{s,0}$ are then added to the q_b base shear flows in the respective cells. A convenient point around which to evaluate the moments is then chosen. The internal moments due to the shear flow are evaluated around this point and set equal to the external moment caused by shear force S_y. From the last moment arm, ζ_0 can be computed, which gives the location of the shear center as in Equation 5.8.

$$S_y \zeta_0 = \oint p q_b\, ds + q_{s,0} \oint p\, ds \tag{5.8}$$

5.2 Forces and Moments

In section 4.1, it is explained how the sum of forces and sum of moments are solved numerically. It will become apparent that the vertical displacement of hinge 1 and hinge 3 is used to acquire three

extra equations necessary to solve the system of reaction forces. Thus, the given deflection is used in the next chapter to find the value and direction of the forces.

In this section, a method is proposed that uses a virtual force to find a certain deflection. This enables an analytical model that can verify the numerical output using a simple baseline equation. Two different load cases are considered as follows. A simply supported beam at the ends with a concentrated load P at any point along the beam (1); and a simply supported beam at the ends with a uniformly distributed load ω (2). For case (1) and (2), the respective maximum deflections are given by Equation 5.9 (Hibbeler, 2014).

$$\delta_{max} = \frac{Pb\left(l^2 - b^2\right)^{3/2}}{9\sqrt{3}lEI} \qquad \delta_{max} = \frac{5\omega l^4}{384EI} \tag{5.9}$$

5.3 Shear Flow and Torsion

Using the shear forces determined in the previous section, the shear flow and torsion can be calculated. For these calculations, one rotates the reference frame as is done in the previous calculation of the moments of inertia. This simplifies the method greatly due to symmetry and will still obtain the same output provided the applied forces are rotated as well.

5.3.1 Shear Flow

From section 5.1, the centroid and moments of inertia are known. Two cuts are made (one in each cell) and the base shear flow q_b is evaluated as if the section were open. Equation 5.10 is used to evaluate the base shear flow.

$$q_s = -\left(\frac{S_z I_{zz} - S_y I_{yz}}{I_{zz} I_{yy} - I_{yz}^2}\right) \int_0^s tz ds - \left(\frac{S_y I_{yy} - S_z I_{yz}}{I_{zz} I_{yy} - I_{yz}^2}\right) \int_0^s ty ds + q_b \tag{5.10}$$

A convenient point to evaluate the moments around is then picked and the internal moments M_b due to the base shear flows is calculated. The contribution from $q_{s,0}$ is added to this and equated to the moment due to the external forces as in Equation 5.11. From this equation, $q_{s,0}$ is derived and its contribution is then added to the base shear flows.

$$M_{ext} = M_b + 2Aq_{s,0} \tag{5.11}$$

5.3.2 Torsion

To find the torsion present in the multi-cell section in the z-y plane, the shear flow contributions present in the skin are summed as in Equation 5.12 (Megson, 2013).

$$T = 2A_{e,I} q_I + 2A_{e,II} q_{II} \tag{5.12}$$

The deflection in the multi-cell structure is then assumed constant for the different cells in the z-y plane. It follows that we can use Equation 5.13 to find the deflection in the z-y plane.

$$\frac{d\theta}{dx} = \frac{1}{2A_r} \oint \frac{q}{Gt_{sk}} ds \tag{5.13}$$

6 | Numerical Model

Since the mechanical behavior of a complex structure can only be described in approximation by an analytical model, a numerical model is needed in order to describe the response of the aileron more accurately. The numerical model is constructed by dividing the complex structure into simpler parts, which are eventually linked to each other numerically. In this chapter, the numerical model of the aileron is explained in detail.

6.1 Area Characteristics

Since a correct area characteristics calculation is crucial for the model accuracy and all subsequent calculation, this chapter takes a close look on how these were calculated in the numerical model. The numerical model uses idealized boom theory to speed up calculations, accepting that a difference in accuracy will surface during model verification. A more in-depth elaboration on the effects of the idealization of the structure can be found under item 3 in chapter 3.

6.1.1 Boom Areas

In the boom idealization, all the relevant area is lumped in the booms. This means the skin contribution for these areas needs to be determined using Equation 6.1. The stringers are equally spaced along the wing box circumference, as stated in Van der Wal and Campen (2018). Since the booms are assumed to be located at the stiffener positions, the areas of these stiffeners need to be added to the skin area contributions of the respective booms. Booms are also assumed to be present at the spar intersection location with the skin. At this spar location, only skin contributions are accounted for. The normal stress ratios necessary to find the boom area due to skin contribution are determined through their respective distances to the symmetry axis, assuming a linear normal stress distribution (Megson, 2013).

$$B_r = \frac{t_{sk} b}{6} \left(2 + \frac{\sigma_{r\pm1}}{\sigma_r} \right) \tag{6.1}$$

Figure 6.1 shows the position of the booms.

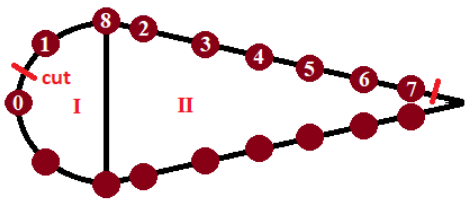

Figure 6.1: The picture shows the location of the booms.

6.1.2 Centroid

The centroid of the idealized section is then calculated using Equation 6.2. The equations expanded on in the subsequent sections are specified for the z-y plane, although they also hold in the other

planes. For convenience in calculation, the z-y plane is assumed to be such that the z-axis is the axis of symmetry through the body (item 1d in chapter 3). This introduces a significant reduction in calculation time and one can still take the angle θ into account in the force vectors.

$$\bar{y} = \frac{\Sigma B_r \tilde{y_r}}{\Sigma B_r} \qquad\qquad \bar{z} = \frac{\Sigma B_r \tilde{z_r}}{\Sigma B_r} \tag{6.2}$$

6.1.3 Moments of Inertia

The moments of inertia are found around the previously determined centroid. Due to boom idealization, the area of the skin is accounted for in the booms. This means the moments of inertia are calculated from the Steiner terms only, resulting in the expressions as seen in Equation 6.3.

$$I_{yy} = \Sigma B z^2 \qquad\qquad I_{zz} = \Sigma B y^2 \qquad\qquad I_{yz} = \Sigma B y z \tag{6.3}$$

When the the z-y plane is shifted as stated in subsection 6.1.2, the section is symmetric around the new z-axis and I_{yz} is zero.

6.2 Forces in Y-Direction

As can be seen from the sum of forces in y-direction and the sum of moments around the x- and z-axis, the system is statically indeterminate for the forces in y-direction. There are 3 unknowns (R_1^y, R_2^y and R_3^y), but only 2 equations available (the sum of forces in y-direction and the sum of moments around the z-axis). Therefore, in order to solve this system analytically, the deflection will be taken into account using Macaulay's method. According to Megson (2013), the double differentiated deflection in z- and y-direction are given as stated in Equation 6.4.

$$z" = \frac{I_{yz}M_z - I_{zz}M_y}{E\left(I_{zz}Iyy - I_{yz}^2\right)} \qquad\qquad y" = \frac{I_{yz}M_y - I_{yy}M_z}{E\left(I_{zz}Iyy - I_{yz}^2\right)} \tag{6.4}$$

Solving for M_y and M_z using Macaulay's method (step functions), the relations as stated in Equation 6.5 are obtained. These relations are based on Figure 2.2 (the geometry of the aileron in the x-z plane) and Figure 2.3 (the FBD-diagram of the system).

$$\begin{aligned} M_z(x) &= R_3^y\left[x - (l_a - x_3)\right] + R_2^y\left[x - (l_a - x_2)\right] + R_1^y\left[x - (l_a - x_1)\right] - \frac{qx^2}{2} \\ M_y(x) &= -P\left[x - \left(l_a - x_2 - \frac{1}{2}x_a\right)\right] - R_2^z\left[x - (l_a - x_2)\right] \\ &\quad - F_I^z\left[x - \left(l_a - x_2 + \frac{1}{2}x_a\right)\right] - R_1^z\left[x - (l_a - x_1)\right] \end{aligned} \tag{6.5}$$

Next, Equation 6.4 is integrated in order to find the deflection in y- and z-direction. For convenience, constants are determined as stated in Equation 6.6. After integration, the relations for the deflection are obtained (Equation 6.7) where the constants of integration are included.

$$C_1 = \frac{I_{zy}}{E\left(I_{zz}I_{yy} - I_{zy}^2\right)} \qquad C_2 = \frac{I_{zz}}{E\left(I_{zz}I_{yy} - I_{zy}^2\right)} \qquad C_3 = \frac{I_{yy}}{E\left(I_{zz}I_{yy} - I_{zy}^2\right)} \tag{6.6}$$

$$\begin{aligned} z &= C_1 \iint M_z(x)\,dx^2 - C_2 \iint M_y(x)\,dx^2 + Ax + B \\ y &= C_1 \iint M_y(x)\,dx^2 - C_3 \iint M_z(x)\,dx^2 + Cx + D \end{aligned} \tag{6.7}$$

Both parts of Equation 6.7 can be solved by combining the boundary conditions for the known deflection at certain x-locations and the sum of forces and moments. The boundary conditions in z-direction are based on the fact that it is given that hinge 1 and hinge 2 are restricted in z-direction (chapter 2). As a result, displacement in z-direction will be zero at both hinges 1 and 2. Concerning the y-direction, it is given that there is a vertical displacement at hinge 1 and hinge 3, d_1 and d_3 respectively. Furthermore, hinge 2 will not move in y-direction: as a consequence, deflection in y-direction at hinge 2 will be zero. The above-mentioned is summarized in Table 6.1. When using the

Table 6.1: Boundary conditions for the deflection in y- and z-direction

$y = d_1$	for	$x = l_a - x_1$	$y = 0$	for	$x = l_a - x_2$	$y = d_3$	for	$x = l_a - x_3$
$z = 0$	for	$x = l_a - x_2$	$z = 0$	for	$x = l_a - x_1$			

boundary conditions for the deflections in y, three equations are generated. Combining these with the sum of forces in y-direction (Equation 4.1) and the sum of moments around the z-axis (Equation 4.2), five equations are generated for a system with 5 unknowns: R_1^y, R_2^y, R_3^y, C and D. Defining matrix Y, vector $\boldsymbol{v}$ and vector $\boldsymbol{m}$ as in Equation 6.8 is the last step in solving the system for the forces in y-direction.

$$
\begin{aligned}
&Y\boldsymbol{v} = \boldsymbol{m} \\
&Y = \begin{bmatrix}
0 & c_3\frac{(-x_1+x_2)^3)}{6} & c_3\frac{(-x_1+x_3)^3)}{6} & -(l_a - x_1) & -1 \\
c_3\frac{(-x_3+x_1)^3)}{6} & c_3\frac{(-x_3+x_2)^3)}{6} & 0 & -(l_a - x_3) & -1 \\
c_3\frac{(-x_2+x_1)^3)}{6} & 0 & c_3\frac{(-x_2+x_3)^3)}{6} & -(l_a - x_2) & -1 \\
1 & 1 & 1 & 0 & 0 \\
x_2 - x_1 & 0 & -(x_3 - x_2) & 0 & 0
\end{bmatrix}, \quad \boldsymbol{v} = \begin{bmatrix} R_1^y \\ R_2^y \\ R_3^y \\ C \\ D \end{bmatrix} \\
&\boldsymbol{m} = \begin{bmatrix}
C_1\left(\frac{-P\left(-x_1+x_2+\frac{x_a}{2}\right)^3}{6} - \frac{R_2^z(-x_1+x_2)^3}{6} - \frac{F_I^z\left(-x_1+x_2-\frac{x_a}{2}\right)^3}{6}\right) - d_1 \\
C_1\left(\frac{-P\left(-x_3+x_2+\frac{x_a}{2}\right)^3}{6} - \frac{R_2^z(-x_3+x_2)^3}{6} - \frac{F_I^z\left(-x_3+x_2-\frac{x_a}{2}\right)^3}{6} - \frac{R_1^z(-x_3+x_1)^3}{6}\right) - d_3 \\
C_1\left(\frac{-P(x_a 2)^3}{6} - \frac{F_I^z\left(-\frac{x_a}{2}\right)^3}{6} - \frac{R_1^z(-x_2+x_1)^3}{6}\right) \\
ql_a \\
-ql_a\left(\frac{l_a}{2} - x_2\right)
\end{bmatrix}
\end{aligned}
\tag{6.8}
$$

6.3 Internal Forces

In order to compute the internal forces, especially the shear forces and the internal moments, the same approach is used as in section 4.1. With Macaulay's method (step functions), a relation for the moment was already obtained as stated in Equation 6.5. In order to find the shear force, the step function of the moment is differentiated as shown in Equation 6.9.

$$
\begin{aligned}
S_y(x) &= \frac{dM_z(x)}{dx} \\
&= R_3^y\left[x - (l_a - x_3)\right]^0 + R_2^y\left[x - (l_a - x_2)\right]^0 + R_1^y\left[x - (l_a - x_1)\right]^0 - qx \\
S_z(x) &= \frac{dM_y(x)}{dx} \\
&= -P\left[x - \left(l_a - x_2 - \frac{1}{2}x_a\right)\right]^0 - R_2^z\left[x - (l_a - x_2)\right]^0 \\
&\quad - F_I^z\left[x - \left(l_a - x_2 + \frac{1}{2}x_a\right)\right]^0 - R_1^z\left[x - (l_a - x_1)\right]^0
\end{aligned}
\tag{6.9}
$$

6.4 Shear and Torsion

Having defined all the relevant geometric properties in section 6.1, these can then be used to determine the effect of the forces acting on the structure. To know the deflections and stresses acting on the structure, it is necessary to determine the shear flow and torsion acting on the structure. The numerical method to obtain these is explained here.

6.4.1 Shear Flows

To determine the shear flows, first two cuts in the structure were made and the cells were evaluated as if they were open. In this way it is possible to find the base shear flow q_b for both cells. Due to the idealization, the shear flow in between booms is constant. In the skins, where the cuts were made, q_b is zero.

The shear flows between each boom are then determined from Equation 6.10. In this equation for the z-y plane, I_{yz} is zero due to symmetry and t_{sk} is zero due to previous idealization. Also due to symmetry, the y-coordinate of the shear center is already known to be 0, so only the z-coordinate of the shear center still needs to be found. This means S_z can be assumed to be zero as well. After determining all shear flows of the cross-section, the moment arms are determined.

$$q_s = -\left(\frac{S_z I_{zz} - S_y I_{yz}}{I_{zz} I_{yy} - I_{yz}^2}\right)\left(\int_0^s t_{sk} z ds + \sum_{r=1}^{n} B_r z_r\right) - \left(\frac{S_y I_{yy} - S_z I_{yz}}{I_{zz} I_{yy} - I_{yz}^2}\right)\left(\int_0^s t_{sk} y ds + \sum_{r=1}^{n} B_r y_r\right) + q_b \tag{6.10}$$

The shear flow at the ribs have to be taken into account. At the rib locations along the x- axis, the moments of inertia changes to account for the extra rib area, by distributing the total rib area evenly to each boom. This change only occurs at the specific locations where the ribs are located.

Each cell is then cut at the leading and trailing edge of the cross section and the section is evaluated from the cut at which $q_b = 0$ using Equation 6.10. In our idealized cells, $t_D = 0$ is assumed.
Subsequently, the cell is closed and the moments are calculated around a convenient point, the hinge point, as the shear flow through the spar can be neglected and the location is at the symmetry line. Next, the torque contributions are summed to find the constant shear flows $q_{0,r}$ using Equation 6.11 and Equation 6.12. The angle of twist at the shear center is 0, so 2 formulas for the torque contribution due to the shear flows can be found, and then with 2 unknowns, $q_{0,1}$ and $q_{0,2}$, and 2 equations for 0 twist, the closed section shear flows are found for each specific loading case.

$$\sum M + \sum_{r=1}^{n} 2A_r q_{0,r} = 0 \tag{6.11}$$

Every cell in the z-y plane is assumed to have the same angle of twist, which is also still unknown. This means one can find an angle of twist expression for each cell with Equation 6.12.

The shear center is the point around which the angle of twist is zero. This means for both cells in the z-y plane, it can be assumed that Equation 6.12 is equal to zero. Because the enclosed area and shear modulus are constant for the individual cells, this equation reduces to $\oint \frac{q}{t_{sk}} ds = 0$ for each cell. These two equations are worked out into expressions for q_{s01} and q_{s02}.

$$\frac{d\theta}{dx} = \frac{1}{2A_r} \oint \frac{q}{G t_{sk}} ds \tag{6.12}$$

A moment equation around the hinge is set up such that the external moment caused by S_y equals the internal moment caused by the shear flows q_s and the torsion from q_{s0}. From the moment arm

from this arbitrary point around which the moments are taken to the point through which the shear force S_y acts, the location of the shear center on the z-axis can be determined. The determination of the shear center isn't necessary, but the closed section shear flows are found as a final step towards finding the shear center, which are necessary.

6.4.2 Torsion

To find the torsion present in the multi-cell section in the z-y plane, the shear flow contributions present in the skin are summed as in Equation 6.13 and the twist equation for each cell is equal to zero, and as such q_I and q_{II} are determined Megson, 2013.

$$T = 2A_{e,I}q_I + 2A_{e,II}q_{II} \tag{6.13}$$

The deflection in the multi-cell structure is assumed to constant for the different cells in the z-y plane. It follows that we can use Equation 6.14 to find the deflection in the z-y plane. The span in the x direction of the aileron is divided into 1000 points, and at every point the internal shear forces are applied on the cross section, along with the torque contribution at that section. In order to apply the distributed load into a use-able torque, the distance between the previous node and the current one is used to find the applied force, which in turn is used to find the applied torque around the hinge line. The angle of twist is then a combination of the internal shear flows and the shear flows due to the external torque, q_I and q_{II}, as shown in equation Equation 6.14.

$$\frac{d\theta}{dx} = \frac{1}{2A_r}\oint \frac{q}{Gt_{sk}}ds + \frac{T_1}{4A_{r1}^2G}\oint \frac{1}{t_{sk}}ds + \frac{T_2}{4A_{r2}^2G}\oint \frac{1}{t_{sk}}ds \tag{6.14}$$

An assumption is made that at the maximum torque loading, the change is angle of twist is the largest, and at the lowest the smallest. The angle of twist at both ends is assumed to be 28 degrees, the maximum deflection, in reality this angle is smaller, but without a constraint for the angle of twist, the point of zero angle change is difficult to determine.

Beginning at 28 degrees, the next point's angle is determined by the angle change due to the shear flow in the initial point, and then the angle change due to torsion is determined by the change in torque loading between the two points. Once the change in the twist angle is found, the new angle at the next point is found by summing the previous angle, in this case 28 degrees, and the change in angle found using the angle of twist formula. This repeats for each point across the span until the angle at each point is found.

Once the angle is known for each point, the leading and trailing edge deflections due to the rotation can be found. These deflections are purely due to torsion and shear flow, the bending deflections are added later to find the full deflection.

7 | Verification

After implementing the numerical solution in code, verification is the only way to get a measure on how accurate this code is. In code verification, the code is checked on whether the model is calculated in the right way. In calculation verification, it is tested whether thing is calculated, so if the right calculations are used. This is done by comparing the numerical model with another model, in this case the analytical one. These models differ in the assumptions they make and can as such test whether these assumptions are valid and whether they introduce reasonable margins of error.

The most insightful way to perform this verification is through slowly working your way up in size of the tested code blocks. This one first tests individual code lines through the debugging tool in Python. Once these initial errors are taken out, the code units are tested. Finally, as these units become bigger, one arrives at the system test. In the end, the entire code needs to be tested, running through all paths of the code at least once. This chapter elaborates on how all of these tests are conducted and what they conclude.

7.1 Code Verification

An initial but crucial step in the verification process is code verification. The goal here is to determine whether the code used is correct.

An initial code verification tests plainly whether the program can run. No judgment on the correctness of the used model can be made from these results: while the code may be correct, results will still not make sense if the implemented equations are wrong. Python's built-in debugging tools like PyCharm make this process fairly straightforward and easy. Here, the compiler can find serious mistakes for you, like syntax errors. Mistakes that will compile, such as an error in parenthesis or running a loop too short, will not be spotted.

A second code-level verification is done manually, by going through the code and checking line by line whether everything makes sense. Problems like typing errors and inconsistencies can thus be resolved. Mistakes that can be compiled are spotted like this as well. Ideally, the code should also run as efficiently as possible; code that is not used should be removed.

These mistakes can come in all sizes and forms: variables can cause issues, as the aerodynamic load variable, q, and the shear force variable, q_s, are very similar. Arrays are going to be used to store variables, and as such it's important that the code uses the correct index, and appends the variables into the array using the correct index as well. The effect and induced errors of discretization that are inevitable in code also need to be accounted for. The size of your mesh, the discretized effect on derivatives and integrations and the inevitable difference in calculation from an analytical model to a numerical one are all present. It is then important to account for these and make their effects satisfactory small while keeping the code size efficient. Many things could go wrong in the process of coding and it is therefore essential to check the code's correctness on a line by line basis.

In the code, code verification has been performed throughout the process of writing it, mainly through line by line analysis and peer evaluation. The Python debugging functions were used to take out compilation errors. Anomalies and inefficiencies were taken out to a level that no obvious mistakes could be spotted in peer review of the code.

7.2 Unit Tests

After code verification, it is necessary to check whether the model and assumptions are reasonable. This is done by comparing the numerical model with an analytical model. Using different equations and assumptions in each model, one can check if the numerical model produces reasonable outcomes. In the above analysis, the goal is to be able to check the numerical model against relatively simple analytical equations that can be performed on paper. As both models will introduce different assumptions, one needs to define what would be a reasonable margin of error between the models in this initial design phase. The reasonable margin depends on the variable being evaluated, for example while the moment of inertia around the y axis is much smaller, more than 20%, the difference between the deflections are much smaller, within 10%. A good margin would be, for the final deflections to be within 10% to 15% of each other.

To reach certain confidence levels on how well your program is working, it is essential that every code unit is tested. While not every possibility or likely anomaly may be tested, a good first estimate is to make sure at least every pathway of your code is explored. Full verification coverage of the code will easily expose some of the more obvious and most problematic mistakes.

For this reason, unit testing must be performed on every function. These then check whether the code output is similar to the analytical output and thus makes sense. This comparison is also used to quantify the effect of assumptions and check their accuracy, like the use of booms in the numerical model. A basic unit test compares the results of both models for a unit for different inputs and assesses the outcomes are satisfactory similar. The accuracy margin should be different depending on the complexity of the considered bit of code. In the following subsections, the verification the different blocks of code is explained.

7.2.0.1 Area Characteristics

The first thing to verify are the area characteristics of the numerical solution. To verify this, the results from the analytical model are compared with the results form the numerical model. In Table 7.1 the results for the centroid location can be found. In Table 7.2 the results for the moments of inertia can be found. In Table 7.1 it can be seen that the for the numerical model the centroid is located 37

Table 7.1: Comparison of the position of the centroid

	Analytical model (from the LE)	**Numerical model (from the LE)**	**Difference**
z-location	243 mm	280 mm	37 mm

mm further in the negative z-direction. This means the numerical model deviates about 13 % from the analytical model. The main reason for this deviation is due to use of idealization. Since only the boom areas are taken into account, this means that in the numerical model more area is located toward the trailing edge of the aileron and therefore the centroid is located closer to the trailing edge.

Table 7.2: Comparison of the moments of inertia

	Analytical model	**Numerical mode**	**Difference**
I_{yy}	8.0016×10^{-5}	5.6943×10^{-5}	2.3073×10^{-5}
I_{zz}	9.936×10^{-6}	10.03×10^{-6}	0.094×10^{-6}

This idealization is also clearly visible in the moments of inertia, as seen in Table 7.2. The moment

of inertia around the z-axis is very accurate (the difference is < 1 %), as is to be expected because the mass distribution stays largely the same. The moment of inertia around the y-axis is off by 28 % from the analytical model. This is significant and needs to be accounted for in further development of this model. The reason for the difference is that the booms significantly shift the weight contribution around the y-axis. This will introduce some errors in other calculations. An underestimated moment of inertia will result in an overestimated normal stress and an underestimated shear flow. The shear load is typically less critical than the normal stress, so overall the numerical model is considered conservative.

Finally, the shear center location is evaluated. The analytical shear center is 15,431cm from the leading edge, the numerical one is 21cm. This difference stems from the idealization of the structure as well: some of the main components in determining the base shear flows necessary for the shear center are the moment of inertia I_{yy} and the skin contributions, both of which are most heavily affected by the boom idealization assumption.

7.2.0.2 Internal and External Forces

The numerical model for force calculation is checked by applying it to previously solved problems that are widely available from previous Mechanics of Materials courses. The code is written such that it can be applied on a variety of problems. As a consequence, the code can be checked on its correctness by using examples with known outcomes.
The method in which this is done is shown in section 5.2. When filling in the values for a certain load P and ω as can be seen in Table 7.3, the deflections can be calculated both by hand and by the numerical model. The results of these methods can be seen in Table 7.4. Note that the values of both the concentrated and distributed load are chosen randomly.
As can be seen in Table 7.4, the numerical model can be considered accurate for computing the reaction forces when a certain deflection is given.

Table 7.3: Values used for verification of the reaction forces

Variable		**Value**
Concentrated load P		46 kN
	Acting on beam of total length l	124 cm
	At location x_P	86 cm
Distributed load ω		8.9 kN/m
	Along the whole length of beam with length l	345 cm

Table 7.4: Comparison of the reaction forces and their resulting deflections

	Analytical Model	**Numerical Model**	**Difference**
δ_{max} for a concentrated load P	$2.6 \cdot 10^{-4} m$	$2.4 \cdot 10^{-4}$	$2.0 \cdot 10^{-5}$
δ_{max} for a distributed load ω	$2.9 \cdot 10^{-3} m$	$2.8 \cdot 10^{-3}$	$1.0 \cdot 10^{-4}$

7.2.0.3 Normal Stress

The normal stress evaluation is given in table Table 7.5.

Table 7.5: Normal stress at the maximum and at the ribs.

	x [mm]	y [mm]	z [mm]	total [Pa]
Maximum	1449	-108.8	-173.9	$1.154 \cdot 10^9$
Rib A	2489	-198.3	10.35	$6.227 \cdot 10^5$
Rib B	1625	-108.8	-173.9	$9.174 \cdot 10^8$
Rib C	1275	-108.8	-173.9	$1.045 \cdot 10^9$
Rib D	1450	-108.8	-173.9	$1.055 \cdot 10^9$

7.2.0.4 Shear Flow

The method of finding the shear flows for both the analytical and the numerical model likely produces most of the discrepancies. The boom idealization of the cross section reduces the bending stiffness of the structure, as mentioned earlier. The moment of inertia, force loading at the cross section and the assumption that the skins carry no normal stresses all have a varying result on the shear flows through the cross section. The idealization assumes that the shear flow remains constant between the booms, while in reality they vary throughout the section. The numerical moment of inertia is lower than the analytical solutions, resulting in higher shear flows throughout the section.

7.2.0.5 Shear Stress

Due to the idealization of the structure, the shear flow is constant between booms. This reduces the computational time, however it also brings some deviation from reality since it is often not linear but quadratic. The magnitude of the shear flow can be slightly higher or lower between the booms, as can be seen in Table 7.6.

Table 7.6: Shear stress at the maximum and at the ribs.

	x [mm]	Booms	total numerical [Pa]	total analytical [Pa]
Maximum	1625	5 - 6	$3.899 \cdot 10^8$	$1.568 \cdot 10^8$
Rib A	2489	4 - 5	$2.128 \cdot 10^8$	$9.072 \cdot 10^7$
Rib B	1625	5 - 6	$3.899 \cdot 10^8$	$1.568 \cdot 10^8$
Rib C	1275	8 - 9	$3.098 \cdot 10^8$	$1.265 \cdot 10^8$
Rib D	1450	8 - 9	$1.329 \cdot 10^8$	$6.874 \cdot 10^7$

7.2.0.6 Von Mises Stress

The Von Mises stresses are evaluated in Table 7.7 and Figure 7.1. The Von Mises stresses are important to see the relation between the normal and shear stresses acting on the aileron, and is calcultated with Equation 7.1. (Megson, 2013)

$$Y = \sqrt{\frac{1}{2}[(\sigma_x - \sigma_y)^2 + (\sigma_y - \sigma_z)^2 + (\sigma_z - \sigma_x)^2] + 3\tau_{xy}^2 + 3\tau_{yz}^2 + 3\tau_{xz}^2} \tag{7.1}$$

Table 7.7: Von Mises stress at the maximum and at the ribs.

	x [mm]	y [mm]	z [mm]	total [Pa]
Maximum	1449	-108.8	-173.9	$1.388 \cdot 10^9$
Rib A	2489	-198.3	10.35	$6.248 \cdot 10^8$
Rib B	1625	-108.8	-173.9	$1.204 \cdot 10^9$
Rib C	1275	-108.8	-173.9	$1.101 \cdot 10^9$
Rib D	1450	-108.8	-173.9	$1.154 \cdot 10^9$

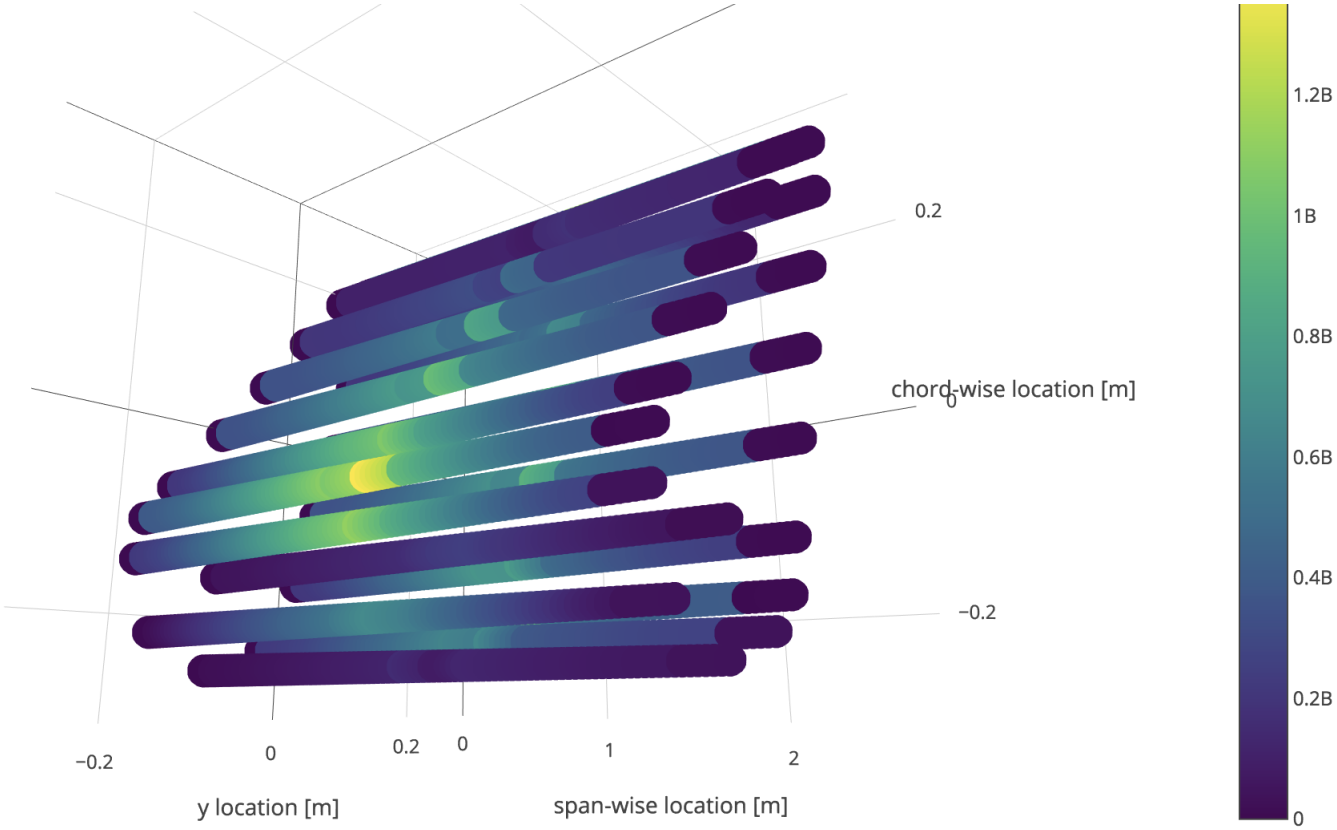

Figure 7.1: Von Mises stress in the aileron

7.2.0.7 Angle of Twist

The idealization for the numerical model assumes the thickness along the outer surface of the cross section is constant, while in the analytical model the thickness changes due to the stringers locally, thus the effect of the torsion is reduced slightly due to an overall, on average, larger thickness. Additionally, the torsion is a function of the span position, x, and so when it comes to solving for θ the torsional shear flow has to be represented as a function of x and then be integrated. In the numerical model a step size is created and the local change in θ is found, however in the analytical the shear flow is integrated across the aileron, resulting in a negligibly small difference.

7.2.0.8 Deflection

The total deflection is the result of two deflection values, the bending deflection and the deflection due to the angle of twist θ. The bending deflection discrepancies depend on the assumptions made. The numerical model uses a boom idealization which results in a lower moment of inertia than the

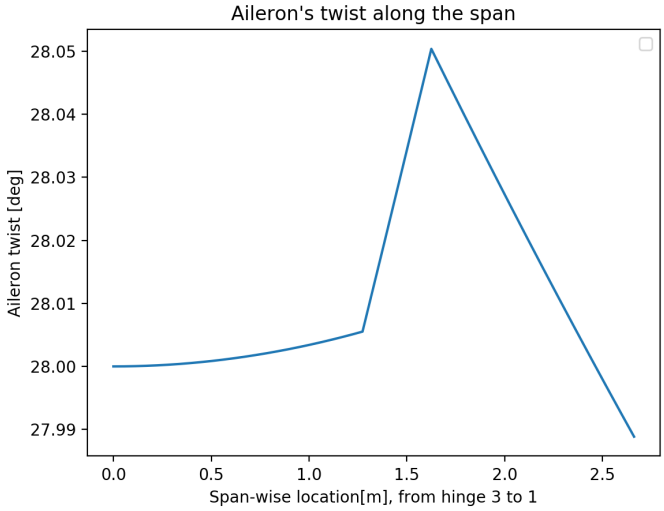

Figure 7.2: Twist of the aileron

analytical model, which means the deflection differs a bit in the numerical model.

The reaction forces also depend on how the beam deflections equations were solved. The reaction forces in hinges 1 and 3 depend on the initial deflection at those points and thus require the moment of inertia, which again, is different due to the effects of idealization. With different deflections and thus different reaction forces at the hinges, the discrepancies snowball, although this affect is small.

The points on the graph in Figure 7.3 indicate the analytical deflections at these locations. As can be seen in Figure 7.3, the deflection computed by the numerical model is fairly accurate compared to the analytical points. While the numerical deflection in the x-z plane may seem very large from Figure 7.4, notice that the scale is very small. These x-z deflections come straight from the equations of motion outlined in the problem analysis and are sufficiently small (within 5 cm for the entire span of the wing).

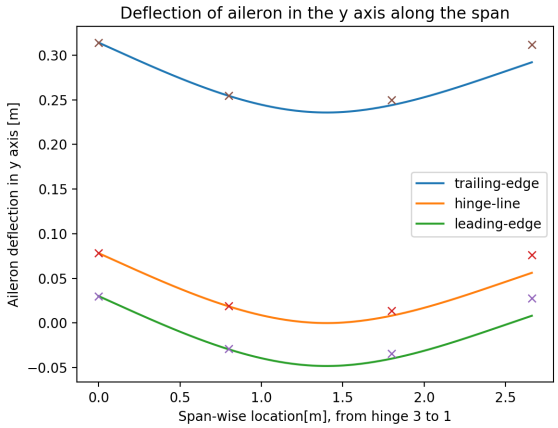

Figure 7.3: Deflection of the aileron in the x-y plane

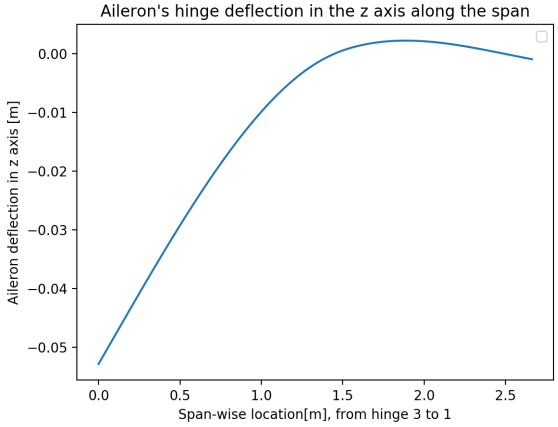

Figure 7.4: Deflection of the aileron in the x-z plane

7.3 System Test

Once every unit is tested, it is still necessary to test whether the code is running correctly. Since the code blocks are already tested, now the path to the outcome is tested. Is the outcome reasonable, not just for the provided input variables but also for anomalies? This can be tested by setting up the system to print intermediary results. If the steps make sense but the outcome does not make sense, intermediary results might easily indicate where errors are created and perpetuated.

Another system test performed is the zero test. Substituting tactically chosen values for zero in combination with the printing of intermediary values of the code is an easy way to show which values are affected and which path the code follows in the flowchart. If the wrong values are affected, it is clear that somewhere in the path between the code blocks an error is made. This technique might be overly simple, but is accurate and precise in spotting the location of errors.

Another system test we performed is the binary search. When output values are off but the code blocks seem fine, the binary search is able to efficiently locate errors. The code is split in two and one looks at which part of the code's values produces wrong results. This part is then split in two again until a small code block remains and the responsible error can be located.

In the code discussed in this report, these system tests were performed throughout the writing process and often unearthed a new range of errors to be dealt with. This eventually resulted in an iterative process of error detection throughout which the code was optimized and detected anomalies were accounted for.

8 | Validation

Validation is the last step in the design process and essential in any model. The validation process checks the model data against experimental data. If the model is inaccurate, the project needs to go back to the fundamental assumptions and change its entire model setup. The validation confirms if the assumptions made are valid and the model can be used to describe the real-world application. In the following sections, the aim is to match the verified data to the validation data and explain any discrepancies.

8.1 Experimental Data

In assessing the experimental data given, one needs to recognize these are not perfect either. The way these are obtained and the environment in which they are obtained is important, as well as the measuring equipment and the errors these induce. Calibration, awareness of design tolerances and careful evaluation, as well as test repetition are therefore important. Therefore some outliers and unusual data can be expected, and random and systematic errors might account for some discrepancies in the validation. In general the data given are assumed to be accurate and obtained in a properly set up experiment. The provided data are the deflections and Von Mises stresses at indicated node points.

8.2 Validation Test

The validation test is executed by plotting the experimental data against the numerical model. In Figure 8.1 the location of the leading and trailing edges are plotted. In red the numerical model, and in black the validation data provided. Since the rotation of the aileron is upward the trailing edge is higher as the trailing edge. As can be seen, the difference between the deflections are within millimeters of each other.

8.3 Accuracy of Results

In validation, the model is expected to differ a bit from the experimental data. This is because the piled up errors from the entire numerical simulation are expected to introduce quite some error, especially in this idealized, initial design phase.

The assumptions made will have the largest effect on the accuracy of the model. An assumption that is too liberal or too conservative can have significant effects. Even if the assumptions result in only a small error, many errors add up. These errors have to be accounted for when comparing the experimental test and the numerical model data.

The idealization of the aileron structure underestimates the bending stiffness and thus the maximum deflection due to bending would result in a higher value from reality. Due to the assumptions about the material and the geometry as perfect material and the aileron considered to be a beam, the

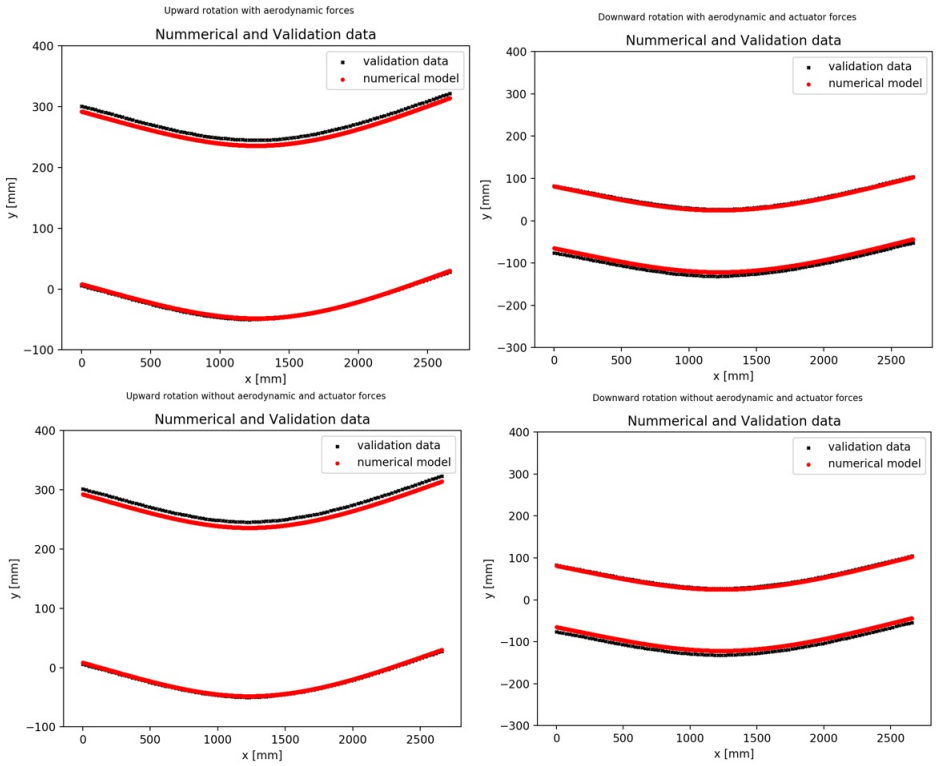

Figure 8.1: Location displacement of leading and trailing edge of the numerical model and the validation data.

deflection would be higher in reality. But also assumptions are made such as the point loads that will have the opposite effect, namely that the deflection would be lower in reality. (Chen, 1975)

Due to the fact that the beam has no constraint for the angle of twist then the location of zero angle change is unknown, an assumption is made that at one end of the aileron, the deflection is 28 degrees. However in reality, this could result in a different value. However the change in deflection due to the twist angle is much smaller than the change due to bending, and as such the difference is only in the order of millimeters at each location. In Table 8.1 the results for absolute maximum deflection at the trailing edge and leading edge are given for the numerical model and the validation data. The maximum deflections only differ millimeters from each other, and as expected, the deflections for the trailing edge of the numerical model are lower than those of the validation data. The validation

Table 8.1: The maximum deflections and their locations for the leading edge (LE) and trailing edge (TE).

Maximum deflection	**Value** [mm]	**Location -x (hinge 3 to hinge 1)** [m]
Validation TE	321.595	0
Numerical TE	314.108	0
Validation LE	28.0042	0
Numerical LE	30.078	0

Von Mises stress distribution produces a maximum stress of of 0.853928 GPa in compression and the numerical model results in a maximum at the same location but with a maximum stress of 1.380 GPa. The result from the numerical model is larger, but not by much. The difference between the numerical and validation data can be attributed to the effect of idealization, the booms take up all the normal stress in the structure and, as such, the stress is higher. Additionally the moment of inertia is lower due to the idealization resulting in further discrepancies in the Von Mises stresses.

8.4 Evaluation

If the validation shows large discrepancies, it is necessary to reconsider the assumptions made. In the model proposed above, idealization will introduce discrepancies with the experimental data. When these discrepancies are considered unacceptable, the idealization assumption will need to be reconsidered.

The deflection values produced by the numerical model do not show any large discrepancies, and as such the assumptions made, and their affects are accounted for. For example, the idealization reduces the bending stiffness and as such the structure is expected to deform more, which it does, albeit by a small margin. The stress values are higher than the validation date due to conservative idealization assumptions.

9 | Conclusion

In this report, an analysis was made of a complex wing box structure. The aim is to satisfactory describe this structure in a model that is an as accurate as possible representation of the physical real-life load conditions.

To achieve this required accuracy, the process of verification and validation is crucial. A numerical model is worthless until it has been tested and checked against reality. These steps, although sometimes tedious and seemingly redundant, are what makes a model viable. Introspection and peer evaluation of the relevance and correctness of a model is essential to any scientific method and aid in the proper understanding and truthfullness of the model.

Therefore, apart from the proposed numerical model, this report also introduces an analytical model to check against. These two models combined introduce a set of assumptions, which one needs to bear in mind when considering its application. The viability of these assumptions and the numerical model are checked in verification. Its applicability is evaluated through validation.

In the verification chapter, several inconsistencies surfaced that would need to be reevaluated in further iterations of this problem subject. Overall, a reasonable accuracy was met and the numerical solution seems viable for an initial aircraft sizing.

In validation, this proposition was proved true: the provided numerical model matches the data set quite well. One needs to conclude that the boom idealization induces the greatest change in accuracy.

As an advice for future consideration of this project, it is essential to iterate the numerical model further. This will need an increasingly accurate analytical model as well, and more insight might still be gained through use of a finite element model.

Bibliography

Chen, W.-F. (1975). *Limit Analysis and Soil Plasticity* (9th ed.). Jan van Galenstraat 335, Amsterdam: Elsevier Scientific Publishing Company.

Hibbeler, R. C. (2014). *Mechanics of Materials* (9th ed.). Upper Saddle River, New Jersey: Pearson.

Kwon, Y.-H. (1998). Transformation of the Inertia Tensor. http://www.kwon3d.com/theory/moi/triten.html.

Megson, T. H. G. (2013). *Aircraft Structures for Engineering Students* (5th ed.). Oxford: Elsevier Aerospace Engineering Series.

van der Wal, W. & Campen, J. (2018). *Structures assignment AE3212 SVV*. Delft University of Technology. Delft.